# Spatial-Temporal Denoised Thermal Source Separation in Images of Compact Pulsed Thermography System for Qualification of Additively Manufactured Metals

Xin Zhang and Jafar Saniie
*ECASP Research Laboratory (http://ecasp.ece.iit.edu)*
*Department of Electrical and Computer Engineering*
*Illinois Institute of Technology, Chicago, IL, U.S.A.*

Alexander Heifetz
*Nuclear Science and Engineering Division*
*Argonne National Laboratory*
*Lemont, IL, U.S.A.*

***Abstract*—We introduce a Spatial-Temporal Denoised Thermal Source Separation (STDTSS) unsupervised machine learning (ML) algorithm for detection of material flaws in additively manufactured (AM) metals using pulsed thermography (PT) images obtained with compact infrared (IR) camera. Quality control of actual AM structures is necessary before their deployment because AM metals can contain defects, such as pores, due to intrinsic features of AM process. The PT nondestructive evaluation (NDE) method is based on recording material surface temperature transients with an IR camera following a thermal pulse delivered on the material surface with a flashlight. The PT method has advantages for NDE of arbitrary size AM structures because the method involves one-sided non-contact measurements and fast processing of large sample areas captured in one image. To reduce the cost and enable in-service NDE in a spatially constrained environment, it is highly desirable to develop PT with a compact and inexpensive IR camera. However, data cube obtained with PT based on compact IR camera suffers from strong thermal noises and loss of features due to relatively low sampling rate. The purpose of the STDTSS algorithm is to compensate for uncertainties detection due to the reduced resolution of low-cost hardware. The STDTSS algorithm consists of spatial and temporal denoising using Gaussian and Savitzky–Golay filtering, followed by the matrix decomposition using Principal Component Analysis (PCA), and Independent Component Analysis (ICA) to automatically detect flaws. We construct a compact PT system based on FLIR A65 camera, and demonstrate the performance of the STDTSS method in the detection of imprinted calibrated defects in AM stainless steel 316L specimens.**

## I. Introduction

Additive manufacturing (AM) of metals is an emerging method for cost-efficient production of low volume custom structures for industries, such as nuclear energy [1,2]. Metals of interest for nuclear applications typically include high-strength stainless steel alloys, such as stainless steel 316L (SS316L). Because of the high melting temperature, AM of SS316L is currently based on the laser powder-bed fusion (LPBF) process [3]. Because of the intrinsic features of the LPBF process, pores can appear in 3D printed metallic structures [4]. With exposure to high temperature and ionizing radiation in a nuclear reactor, the pore can potentially become a seed for fatigue cracking [5]. Because of stringent safety requirements, each AM metallic structure needs to be qualified through nondestructive examination before deployment in a nuclear reactor. If a defect is discovered, either flaw mitigation with heat treatment can be performed, or the part could be disqualified from service.

Typical porosity defects observed in LPBF manufacturing consist of spheroidal-shape keyhole pores caused by excessive laser power, irregular-shape lack of fusion (LOF) pores caused by insufficient laser power, and spherical gas pores caused by trapping of gas in solidifying melt pool. Sizes of pores depend on the quality of the LPBF process. Typical sizes of keyhole and LOF pores in tens to hundreds of microns, while gas pores sizes are on the order of a few microns. Prior studies indicate that larger size pores located closer to the surface are more likely to cause fatigue crack initiation. High-resolution imaging with X-ray or neutron computed tomography (CT) can be used for imaging pores in small coupons to evaluate the quality of the LPBF process. However, applications of X-ray or neutron CT to NDE of actual AM structures are limited because of the large size, lack of symmetry, and complex shapes of AM structures. Ultrasonic testing is scalable with structure size but faces challenges because the rough surfaces, characteristic of AM structures, affect the probe coupling. For high-resolution ultrasonic tomography, imaging of large structures is time-consuming because of point-by-point raster scanning of specimens [6].

The approach to NDE of AM structures discussed in this paper is Pulsed Thermography (PT) imaging, which offers several potential advantages because the measurements are one-sided, non-contact, and scalable to arbitrary size structures [7]. The PT method consists of recording material surface temperature transients with an infrared (IT) camera, following deposition of thermal impulse on the material surface with a flash lamp. In prior studies, we have demonstrated PT performance in the detection of calibrated imprinted defects in SS316L specimens produced with the LPBF method. In general, high-resolution imaging in PT requires expensive IR cameras

with low-noise cooled semiconductor detectors [8]. The cost of the NDE system adds to the overall cost of AM process. In addition to cost considerations, the size of the high-end camera places constraints on the application of PT in in-service NDE in a spatially constrained environment [9]. Therefore, it is highly desirable to develop a PT system based on a compact and inexpensive IR camera. However, a compact lower-cost IR camera, typically consisting of an uncooled microbolometer detector array, suffers from stronger thermal noise and offers lower sensitivity, and lower frame rate. These performance characteristics limit compact PT system capability in the detection of defects in AM structures. [10].

Advances in machine learning (ML) and image processing can potentially compensate for reduced performance characteristics in IR imaging sensor hardware [11]. However, this requires developing ML algorithms that perform a de-noising function without introducing blur into images. Existing ML-based approaches are targeted to processing thermal images obtained with a high-end IR camera. For example, Independent Component Analysis (ICA) can enhance the visibility of features but is computationally expensive and time-consuming [11]. Neural Learning Blind Source Separation (NLBSS), spatial-temporal blind source separation (STBSS), and spatial-temporal sparse dictionary learning (STSDL) methods which we developed recently enhance detection of features in a data-efficient manner, but performs best with lower-noise high-end IR camera [11]. Pulsed Phase Thermography (PPT) [12], can improve feature detection in frequency spectra using Discrete Fourier Transform but is vulnerable to high-frequency noise [12]. In recent work, we have investigated de-noising thermal images using additive white Gaussian noise (AWGN) model of IR camera noise. We developed a sparse coding-related K-means singular value decomposition (SC K-SVM) ML algorithm for removing AWGN from PT images obtained with a compact IR camera without blurring the images.

In this paper, we develop Spatial-Temporal Denoised Thermal Source Separation (STDTSS) ML algorithm for processing PT images obtained with a compact IR camera, which includes de-noising and feature detection. The STDTSS involves spatial and temporal denoising using Gaussian filtering [13] and Savitzky–Golay filtering [14], followed by the matrix decomposition using Principal Component Analysis (PCA) [13], and Independent Component Analysis (ICA) [15], to automatically detect flaws in images. In STDTSS, a 2D Gaussian filter is designed to spatially denoise high-frequency components in thermography images, while preserving signatures of material defects. In addition, a 7-point Savitzky–Golay filter is utilized to smooth each pixel in time sequences without distorting the PT signal intensity. Next, PCA is used to decompose thermography data into principal features, which are fed ICA implemented as a two-layer neural network structure. The ICA is optimized with a fast fixed-point algorithm [15] to further decompose thermography data to speed up detection. The advantage of STDTSS is data-efficient which requires little computation and memory space for fast processing of image quality control of AM structures. We demonstrate the performance of the STDTSS algorithm in the detection of calibrated imprinted defects in SS316L specimens using a PT system based on a compact IR camera.

## II. Methodology

### A. Pulsed Thermography Imaging System

Figure 1(a) and Figure 1(b) show the schematic depiction and the experimental laboratory of the PT system setup, respectively. The PT system illuminates the specimen with a high-energy flash lamp, which rapidly deposits heat on the surface of the material. In the setup shown in Figure 1, a Balcar ASYM 6400 white light flash lamp is used to deliver a flash of 6400J with a flash duration of 2ms. The pulse trigger sends a signal to the capacitor to discharge the circuit to activate the white light flash lamp. The same trigger activates a megapixel fast-frame IR camera, which records time-resolved images of the material surface temperature distribution $T\ (x, y, t)$. Therefore, the acquired data cube consists of a sequence of 2D thermography images at consecutive time instants.

In the work described in this paper, we use a relatively low-cost compact FLIR A65 camera. This camera has dimensions of 295 × 200 × 105 mm (L × W × H). The detector of the camera is a focal plane array uncooled vanadium oxide microbolometer, which has detection sensitivity (noise equivalent temperature detection) of 50mK and operates in the spectral range 7.5-13 $\mu m$. The camera has a spatial resolution of 640 × 512 pixels with a 30 Hz frame rate.

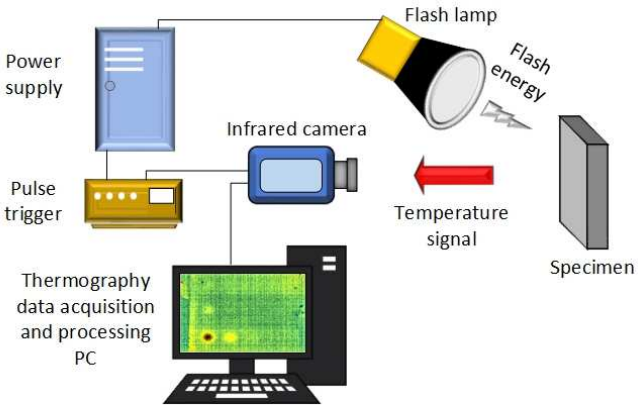


(a)

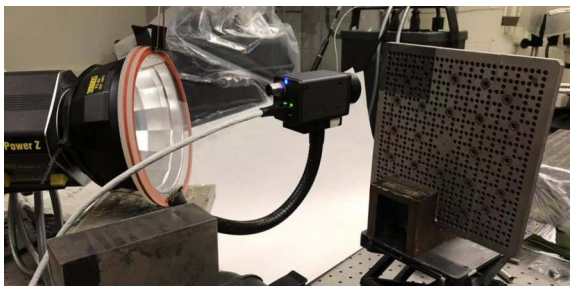

(b)

Figure 1. (a) Schematics of pulsed thermography setup (b) Experimental laboratory setup utilizing compact FLIR A65 camera.

As heat is deposited with a flash lamp the surface starts diffusing into the material bulk, presence of low-density internal material inclusions is revealed through the appearance of local temperature “hot spots” on the surface. This effect occurs because low-density defects have lower thermal diffusivity compared with solid material. The defects act as thermal resistances and slow down thermal diffusion, which causes temperature differences on the material surface between regions

of defects and non-defects. The feature of temperature difference on the material surface is used for internal defect detection. However, the feature intensity is distorted due to thermal imaging noises, uneven heating of specimens, and a low sampling rate of an inexpensive IR camera. The objective of this paper is to demonstrate that STDTSS compensates for PT image artifacts to enable the detection of flaws.

### *B. Spatial-Temporal Denoised Thermal Source Separation*

The STDTSS algorithm is partly based on a previously developed NLBSS algorithm, which was used in PT image analysis [8]. Because of the stronger imaging noises and a lower sampling rate of the compact IR camera, we incorporate several image denoising features into the STDTSS algorithm. In particular, we design a Gaussian spatial filter and a 7-point Savitzky–Golay temporal filter as preprocessing steps to remove IR imaging noises in space and time. Next, PCA is used to decompose thermography data into principal features, which are fed into ICA implemented as a two-layer neural network structure. The ICA aims to classify and separate the thermography source signals, which correspond to image regions of defects, non-defects, and noise. Each thermography source signal exhibits different temperature evolution during the transient response recorded with the PT system. We reconstruct the Thermal Source Image (TSI) from STDTSS to display image regions of defects to detect flaws. The flow chart of the STDTSS algorithm is shown in Figure 2.

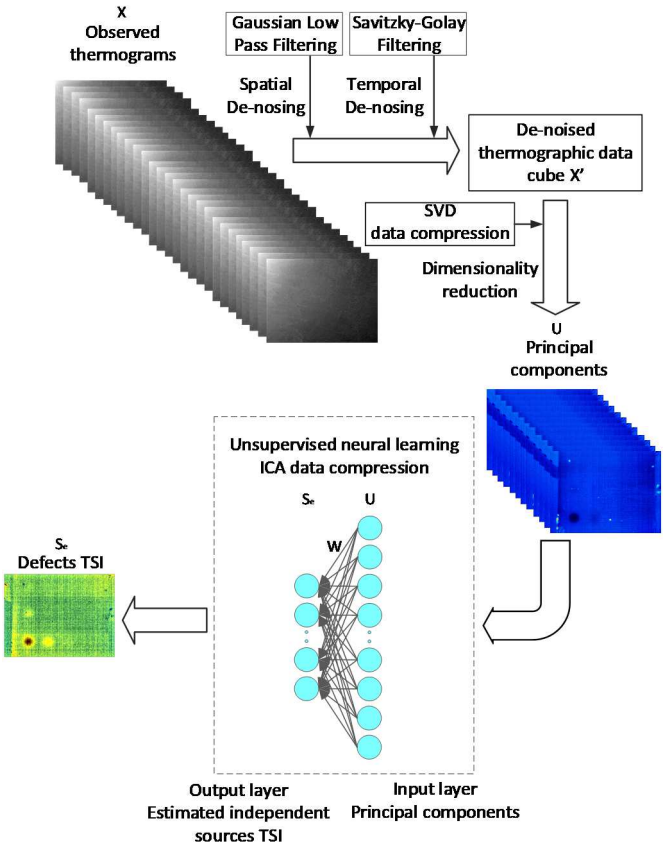


Figure 2. Flowchart of STDTSS algorithm.

The flowchart in Figure 2 shows that the observed thermograms X are mixed with different thermography source signals which need to be denoised and separated. The Gaussian low pass filter followed by the Savitzky–Golay filter is used to remove noises from thermograms X in space and time. Next, the denoised thermography data cube X′ is decomposed with PCA which is implemented as Singular Value Decomposition (SVD) to obtain principal thermography features U. The principal components U are fed as inputs to the neural learning-based ICA for further decomposition and classification to estimate the thermal source signals of defects $S_e$, which are TSI of defects. Here W is the separation matrix used to estimate the TSI.

*a) Gaussian Spatial Denoising:* We design a 3×3 Gaussian low pass filter that spatially removes thermography noises. This 2D Gaussian function is given as:

$$G(x,y) = \frac{1}{2\pi\sigma^2} e^{-\frac{x^2+y^2}{2\sigma^2}} \tag{1}$$

A 3×3 normalized convolution matrix with $\sigma = 0.84$ is produced by the Gaussian function in Equation (1). The matrix H is used to smooth out the observed thermography images using the convolution process while preserving the signatures of material defects. The matrix H is given as:

$$H = \begin{matrix} 0.06 & 0.13 & 0.06 \\ 0.13 & 0.25 & 0.13 \\ 0.06 & 0.13 & 0.06 \end{matrix} \tag{2}$$

To quantify the denoising performance of the Gaussian spatial filter, we calculate the peak signal-to-noise ratio (PSNR):

$$PSNR = 10log_{10}\left(\frac{1}{MSE}\right) \tag{3}$$

Where the MSE stands for the Mean Squared Error between the observed thermography image and Gaussian denoised thermography image. Using Equation (3) for observed thermography images and Gaussian denoised thermography images, we obtain an enhancement of PSNR=40.72dB.

*b) Savitzky–Golay Temporal Denoising:* Savitzky-Golay filter is a digital filter using selected convolution coefficients for smoothing the temporal data [14]. In PT, each pixel in thermography image acts as a temporal signal and consists of a set of points $(x_j, y_j)$, where $x_j$ represents the $j^{th}$ time instant and $y_j$ represents the corresponding pixel intensity. These points are noisy in the time domain due to thermal imaging noises [10] but are smoothed by a group of $m$ convolutional coefficients $C_i$ using the following:

$$Y_j = \sum_{i=\frac{1-m}{2}}^{\frac{m-1}{2}} C_i y_{j+i} \tag{4}$$

Where $\frac{m-1}{2} \le j \le n - \frac{1-m}{2}$, and $n$ is the number of observed thermography images. In this paper, we use the 7-point (m = 7) quadratic polynomial convolution coefficients (-2/21, 3/21, 6/21, 7/21, -2/21, 3/21, 6/21) [14] to enhance the precision of data without distorting the PT signal.

*c) Neural Learning-Based Matrix Decomposition:* In order to detect flaws, the denoised thermography data cube $X'$

is decomposed with SVD to extract principal features ($U$) of defects by removing non-relevant information, such as uneven heating due to flashlamp pulse incident at an angle on the material surface (see Figure 1). Next, the principal features are used as inputs to train the neural learning-based ICA to separate image regions containing signatures of defects from image regions that do not contain any material defects. After the separation matrix $W$ is trained using ICA, this matrix is applied to detect flaws by separating the mixed thermograms into TSIs of defects. This neural learning-based ICA consists of one input layer (principal features $U$), and one output layer (estimated source signal $S_e$). The input layer has 20 neurons, equal to the number of principal components. The output layer has 8 neurons, equal to the number of independent components. The nonlinearity function "pow3" ($g(u) = u^3$) [15] is used as the activation function to optimize training with a fast fixed-point algorithm [15] for robust convergence. In addition, the reverse entropy [15] is applied as the objective function to measure the non-Gaussian. We train this two-layer neural network with 100 epochs to estimate the TSI of defects.

## III. Experimental Results

To evaluate the performance of the STDTSS in the detection of flaws using a compact IR camera, we recorded PT images of AM SS316L plate. This plate contains calibrated imprinted internal defects in the form of hemispherical cavities with trapped un-sintered powder. The defects were created when the specimen was fabricated with the LPBF method [9]. Figure 3(a) shows a 3D rendering of hemispherical low-density porosity defects imprinted in AM SS316L specimen. Figure 3(b) shows the photograph of AM SS316L specimen plate (Length×Width×Thickness: 154 mm × 72 mm × 10 mm).

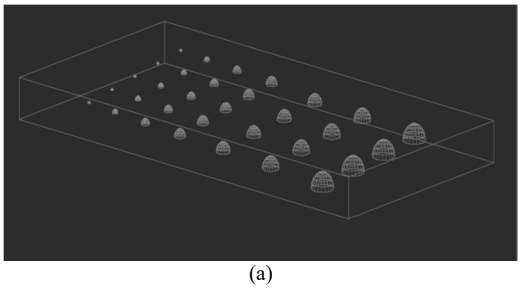

(a)

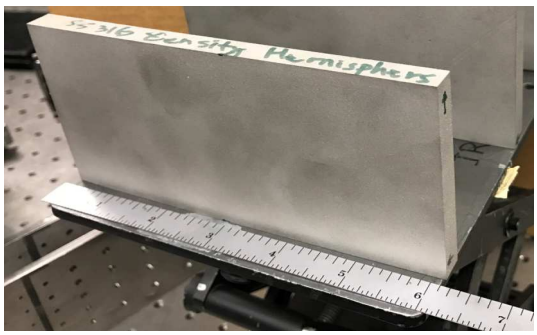

(b)

Figure 3. (a) 3D rendering of hemispherical low-density porosity defects imprinted in AM SS316L specimen (b) Photograph of AM SS316L specimen plate manufactured with the LPBF method.

A drawing with a labeling scheme of diameters and depths of the imprinted defects is shown in Figure 4(a). Note that the depth of an internal hemisphere is defined as the distance from the flat plate surface to the top of the hemisphere. The drawing shows that there are two patterns of defects imprinted into the plate. One pattern has larger defects with diameters Ø = 5, 6, and 8 mm and depths d = 2, 3, 4, and 5 mm. The other one has smaller defects with diameters Ø = 1, 2, 3, and 4 mm and depths d = 1, 2, 3, 4, and 5 mm. Referencing a defect with notation (Ø8, d5) implies that a defect with 8 mm diameter is located at 5 mm depth. The diameters of defects increase along the lines parallel to the longer side of the plate, while the depth along these lines is constant. The depth of defects increases along the lines parallel to the shorter side of the plate, while the diameter is fixed along these lines.

### A. Detection of Larger Defects

In the first experiment, PT imaging was performed on the pattern with larger defects of the AM SS316L plate, which is shown with the red box in Figure 4(a). Figures 4(b), 4(c) show the observed thermography frame and the estimated TSI of defects from STDTSS, respectively. The red dashed line oval in Figure 4(a) shows which of the imprinted defects were detected. Defects (Ø8, d2), (Ø8, d3), and (Ø6, d2) can be clearly seen, while defects (Ø8, d4), (Ø6, d3), and (Ø5, d2) are detected with relatively lower confidence.

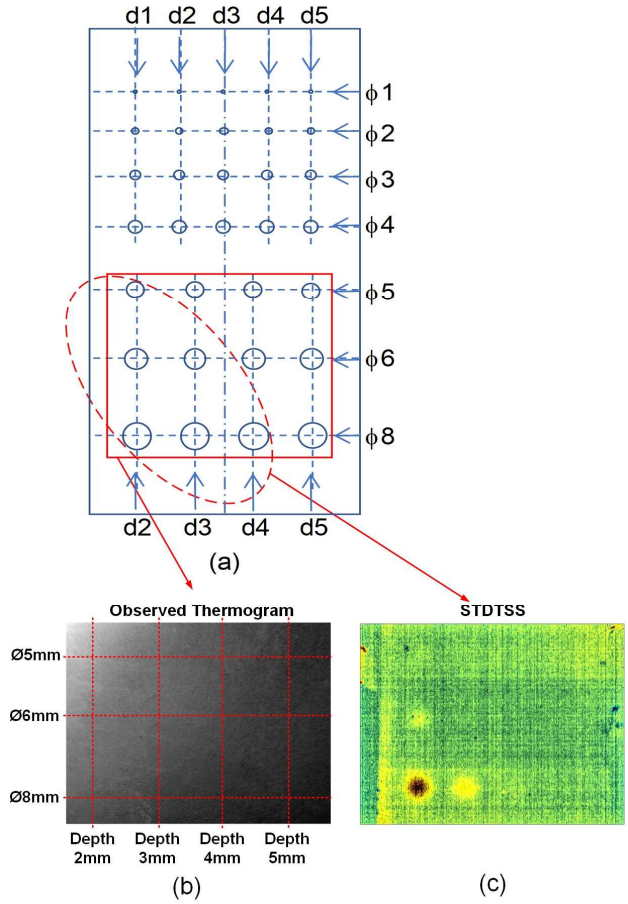


Figure 4. Results of detection of larger defects in SS316L specimen. (a) Area of the plate, (b) Raw thermogram, (c) Estimated TSI with STDTSS.

### B. *Detection of Smaller Defects*

In the second experiment, we repeated PT measurements with the smaller pattern of defects imprinted into the AM SS316L plate. Figures 5(b) and 5(c) show the observed thermography frame and the estimated TSI of defects from STDTSS, respectively. The red dashed line oval in Figure 5(a) shows which of the imprinted defects were detected. Defects (Ø4, d1) and (Ø3, d1) can be clearly seen, while defects (Ø2, d1) and (Ø1, d1) are detected with relatively lower confidence.

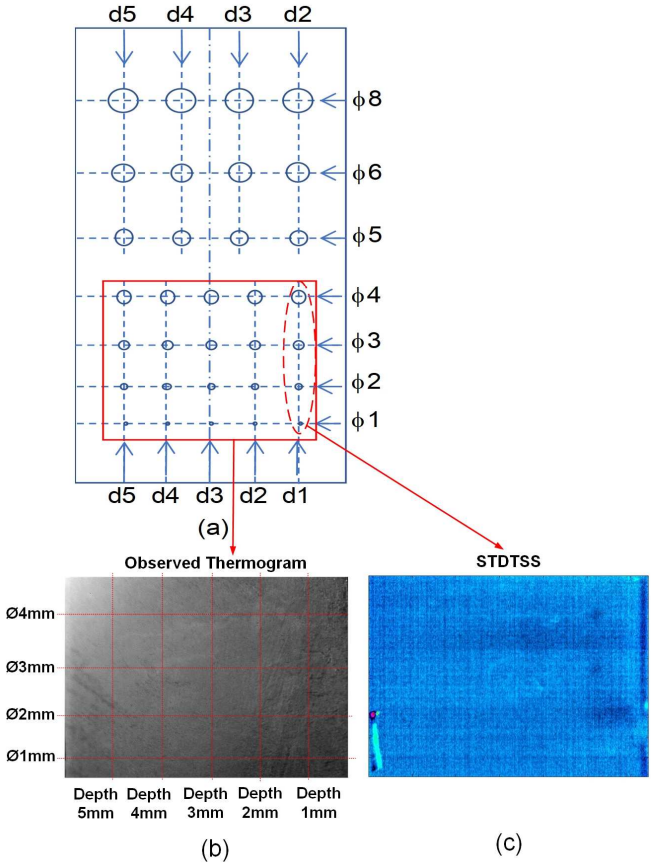


Figure 5. Results of detection of smaller defects in specimen SS316L specimen. (a) Area of the plate, (b) Raw thermogram, (c) Estimated TSI with STDTSS.

## IV. Conclusion

In this paper, we developed an unsupervised ML-based STDTSS algorithm for the nondestructive detection of subsurface defects and qualification of AM structures with a compact PT system. While a compact PT system has advantages in low cost and compatibility with in-service use, the drawback is strong thermal noise and low frame rate of compact IR camera with microbolometer detector. In STDTSS, a 2D Gaussian filter is designed to spatially denoise high-frequency components in thermography images while preserving signatures of material defects. In addition, a 7-point Savitzky–Golay filter is utilized to smooth each pixel in time sequences without distorting the PT signal intensity. Next, PCA is used to decompose thermography data into principal features, which are fed into ICA implemented as a two-layer neural network structure. The ICA is optimized with a fast fixed-point algorithm to further decompose thermography data to speed up detection. The STDTSS is data-efficient which requires little computation and memory space for fast analysis and qualification of AM structures. Performance of the STDTSS algorithm was demonstrated in imaging of an AM structure with a compact PT based on FLIR A65 camera. An AM SS316 plate used in the imaging study contained calibrated internal hemispherical defects with un-sintered powder, which were imprinted when the specimen was fabricated with the LPBF process. To further enhance flaws detection, future work will involve optimizing the STDTSS, for instance, utilizing the sparse PCA, non-linear PCA to decompose thermograms.

## V. Acknowledgment

This work was supported in part by the US Department of Energy, Office of Nuclear Energy, Nuclear Energy Enabling Technology (NEET) Advanced Methods of Manufacturing (AMM) program, under contract DE-AC02-06CH11357.

## References

[1] L. Scime, D. Siddel, S. Baird, V. Paquit. (2020). "Layer-wise anomaly detection and classification for powder bed additive manufacturing processes: A machine-agnostic algorithm for real-time pixelwise semantic segmentation," *Additive Manufacturing*, Volume 36.

[2] X. Lou, D. Gandy. (2019). "Advanced Manufacturing for Nuclear Energy," *JOM*, Volume 71.

[3] S. A. Khairallah, A. T. Anderson, A. Rubenchik, W. E. King. (2016). "Laser powder-bed fusion additive manufacturing: physics of complex melt flow and formation mechanisms of pores, spatter, and denudation zones," *Acta Materialia*, Volume 108.

[4] A. Heifetz, D. Shribak, X. Zhang, J. Saniie, Z.L. Fisher, T. Liu, J.G. Sun, T. Elmer, S. Bakhtiari, W. Cleary. (2020). "Thermal tomography 3D imaging of additively manufactured metallic structures," AIP Advances, Volume 10.

[5] M. D. Sangid, P. Ravi, V. Prithivirajan, N. A. Miller, P. Kenesei, J. Park. (2019). "ICME Approach to Determining Critical Pore Size of IN718 Produced by Selective Laser Melting," *JOM,* Volume 72.

[6] X. Zhang, B. Wang, J. Saniie. (2020). "Deep Convolutional Neural Networks Applied to Ultrasonic Images for Material Texture Recognition," *2020 IEEE International Ultrasonics Symposium*.

[7] X. Zhang, J. Saniie, A. Heifetz. (2020). "Detection of Defects in Additively Manufactured Stainless Steel 316L with Compact Infrared Camera and Machine Learning Algorithms," *JOM,* Volume 72.

[8] X. Zhang, J. Saniie, A. Heifetz. (2020). "Neural Learning-Based Blind Source Separation for Detection of Material Defects in Pulsed Thermography Images," *2020 IEEE International Conference on Electro Information Technology (EIT).*

[9] A. Heifetz, X. Zhang, J. Saniie, D. Shribak, T. Elmer, S. Bakhtiari, B. Khaykovich, W. L Cleary. (2020). "Second Annual Progress Report on Pulsed Thermal Tomography Nondestructive Examination of Additively Manufactured Reactor Materials," Argonne National Laboratory ANL-20/62.

[10] C. Ibarra-Castanedo, A. Bendada and X. Maldague. (2007). "Thermographic image processing for NDT," *IV Conferencia Panamericana de END.*

[11] X. Zhang, J. Saniie, W. Cleary, A. Heifetz. (2020). "Quality Control of Additively Manufactured Metallic Structures with Machine Learning of Thermography Images," *JOM*, Volume 72.

[12] E. D'Accardi, F. Palano, R. Tamborrino, D. Palumbo, A. Tatì, R. Terzi, U. Galietti. (2019). "Pulsed Phase Thermography Approach for the

Characterization of Delaminations in CFRP and Comparison to Phased Array Ultrasonic Testing," *Journal of Nondestructive Evaluation*, Issue 1.

[13] X. Zhang, T. Gonnot, J. Saniie. (2017). "Real-Time Face Detection and Recognition in Complex Background," *Journal of Signal and Information Processing*, Volume 8.

[14] A. Gorry. (1990). "General least-squares smoothing and differentiation by the convolution (Savitzky–Golay) method," *Anal. Chem.*

[15] A. Hyvärinen. (1999). "The Fixed-Point Algorithm and Maximum Likelihood Estimation for Independent Component Analysis," *J. Neural Processing Letters,* Volume 10.